Ultramicroscopy 182 (2017) 17–27

Contents lists available at ScienceDirect

Ultramicroscopy

journal homepage: www.elsevier.com/locate/ultramic

Improved simulation based HR-EBSD procedure using image gradient based DIC techniques

Jon Alkorta[a,*], Matthieu Marteleur[b], Pascal J. Jacques[b]

[a] CEIT and TECNUN (University of Navarra), P° de Manuel Lardizabal 15, Donostia 20018, Spain
[b] Université catholique de Louvain, Institute of Mechanics, Materials and Civil Engineering, IMAP, Place Sainte Barbe 2, Louvain-la-Neuve B-1348, Belgium

ARTICLE INFO

Article history:
Received 13 September 2016
Revised 29 May 2017
Accepted 12 June 2017
Available online 14 June 2017

ABSTRACT

Conventional HR-EBSD is attracting much interest due to its ability of measuring relative crystal misorientations and microstresses with great accuracy. However, this technique needs the use of simulated patterns in order to get absolute values of crystal orientation and stresses and thus expand its use to intergranular analyses. Simulation-based approaches have shown many limitations due to the poor correlation with the real patterns specially when Bragg simulations are considered. This paper presents an improved algorithm based on gradient-based correlation techniques that makes simulation-based HR-EBSD possible. Based on this new algorithm, a new pattern center calibration procedure is proposed and validated. Also, a new hybrid procedure that combines simulation-based HR-EBSD with conventional HR-EBSD is presented that enables an absolute determination of both orientations and stresses with improved accuracy. The hybrid HR-EBSD is used to analyze the martensitic transformation induced by plastic deformation in an as-quenched Ti-12wt.%Mo alloy.

1. Introduction

Hough-based algorithms have been traditionally used to index Kikuchi patterns in conventional EBSD [1,2]. This method is indeed very easy to implement, fast and its resolution is about a few tenths of a degree.

With the continuous increase of computing power, more accurate and sophisticated digital image processing techniques have been recently adapted to EBSD indexing [3–8]. Wilkinson et al. [3–6] have shown that an important increase in angular resolution can be obtained if digital image correlation (DIC) techniques are employed. These correlation techniques can detect image shifts with subpixel resolution leading to an orientation resolution of about 10^{-4} radians. Such a huge improvement in the angular resolution also allows the detection of small lattice distortions due to elastic strains with similar resolution.

However, the so called HR-EBSD technique, since it is basically a DIC technique, needs a reference Kikuchi pattern from which all the misorientations and elastic strains will be derived. As a consequence, only relative measurements can be obtained since a specific real EBSD pattern is considered as the reference pattern. Moreover, if misorientation angle with respect to the reference pattern becomes too large (about some degrees), the patterns differ too much to be analyzed directly by a DIC technique. Maurice et al. and Britton et al. have tried to extend the use of relative HR-EBSD to higher misorientations using a finite deformation framework [9] or by remapping techniques [10] with good results up to misorientations of the order of 10°. However, relative HR-EBSD is still limited to intragranular misorientations and microstrains.

As an alternative to the aforementioned technique, Villert [11], Kacher et al. [12,13] and Fullwood et al. [14] used simulated kinematic patterns as reference patterns and compared them to real patterns through DIC techniques to solve in an iterative way the absolute orientation and absolute stress state of the crystal. However, this simulation based HR-EBSD technique also presents some limitations carefully addressed by Britton et al. [15]. They can be summarized as follows: (1) Optical aberrations in the compact lenses used for pattern capture can result in artificial image shifts between experimental and simulated EBSP; (2) The use of a kinematic simulation can result in errors in the measured shifts, particularly at zone axis and high structure factor bands, due to large intensity variations whereas dynamical models are computationally demanding; (3) An accurate measurement of the experimental geometry (pattern center location) must be known to avoid artifacts in the stress state and misorientations (phantom stresses).

In the present paper, we present three significant advances with respect to the state-of-the-art simulation-based HR-EBSD procedure, solving some of the aforementioned problems. Firstly, we

* Corresponding author.
E-mail address: jalkorta@ceit.es (J. Alkorta).

http://dx.doi.org/10.1016/j.ultramic.2017.06.015
0304-3991/

propose a DIC technique based on image gradients (GB-DIC) that improves the cross-correlation procedure in simulation-based HR-EBSD. Secondly, and based on the above GB-DIC technique, we propose a new pattern center (PC) calibration procedure with minimum stress-related assumptions. Thirdly, we propose a hybrid algorithm (combining the improved simulation-based and real-pattern based HR-EBSD) to extend the use of HR-EBSD to absolute measurement of orientations and elastic strains both in intragranular or intergranular scenarios.

2. Gradient-based DIC for simulation-based HR-EBSD

As commented above, Bragg (kinematic) simulations allow the construction of EBSPs in a computationally efficient way. However, the overall intensities, especially in the neighborhood of a zone axis, are far from the actual intensities of real EBSPs. Dynamical simulations, albeit more accurate, require long computational times (each pattern may take about an hour to be generated on a modern desktop computer [16]).

The algorithm proposed here is similar to the approach of Villert et al. [11]. It is based on the Bragg condition used to determine band locations, together with a modified band profile to emulate excess and deficiency lines. Thus, the intensity of the simulated EBSP is given by the additive contribution of each diffracting plane according to its structure factor, weighted in a very simplistic way by the following criterion: the intensity of the pixel is weighted by 0.8 if it lies within $\sin\theta_B < \sin\theta < 1.2\sin\theta_B$ and by 1.2 if it lies within $0.8\sin\theta_B < \sin\theta < \sin\theta_B$ (where θ is the angle to the corresponding crystal plane and θ_B is the Bragg angle). This modified Bragg model is of course still insufficient to simulate with high accuracy the intensities of an EBSP. In order to improve the fitting quality, a new GB-DIC procedure is proposed, different from the conventional DIC procedure. GB-DIC algorithm is based on the approach suggested by Tzimiropoulos et al. [17]. From an EBSP image, a new image (gradient image) is created based on the intensity gradients in the following form:

$$G(x,y) = \frac{\partial I(x,y)}{\partial x} + i\frac{\partial I(x,y)}{\partial y} \tag{1}$$

where $I(x, y)$ is the intensity of the EBSP image (either experimental or simulated) and i is the imaginary unit (see Fig. 1). The cross-correlation image can be obtained from the Fourier transform of the gradient image of a real ($\hat{G}_{real}$) and a simulated ($\hat{G}_{simu}$) EBSP as follows:

$$C_{ij} = F^{-1}\left(\hat{G}_{real}\,\hat{G}^{*}_{simu}\right) \tag{2}$$

where F^{-1} is the inverse Fourier transform and $\hat{G}^{*}_{simu}$ is the complex conjugate of $\hat{G}_{simu}$. The peak position in C_{ij} corresponds to the image shift between the two images. According to Tzimiropoulos et al., this kind of transformation brings a more robust and accurate estimation of image translations, rotations and scale changes between images. Moreover, this image transformation leads to a pair of complex images where the Kikuchi lines are visibly highlighted and the overall background intensities are flattened. As a consequence, the quality of the fitting (peak height to background ratio in the FFT correlation image) is largely increased as shown in Fig. 2. A more robust fitting of kinematically simulated EBSPs is then possible.

The approach is, in principle, also suitable for comparing two experimental patterns. However, the main objective of this approach is to highlight the Kikuchi band edges in order to decrease the relevance of the intensity of the bands in the cross-correlation procedure. This is important when comparing simulated vs experimental patterns but probably less important when comparing two experimental patterns.

Image filtering has been shown to be critical for an accurate HR EBSD procedure. Wilkinson et al. [4] studied different filtering parameters and finally applied a Hamming-like window in order to prevent aliasing problems and a low-pass filter in the frequency domain to remove noise. In this case, with the aim of highlighting the benefits of the gradient-based procedure, no windowing was considered and only a low-pass filter was applied (equivalent to the one proposed by Wilkinson et al. [4]) with a double objective: first, remove the residual noise from the EBSP image; and second, to smooth down the edges of the Kikuchi bands in the simulated pattern.

Peak position was determined with subpixel accuracy by applying a 2D gaussian fitting to the points within a radius of 2.5 pixels around the maximum.

In order to extract the deformation gradient that relates the real and simulated EBSPs, both images are divided into 32 uniformly distributed regions of interest (ROIs) with size 256×256 pixels. The shift between every pair of ROIs is calculated from the GB-DIC procedure described above. The deformation gradients (with the limitations commented below) that relate both crystals can then be accurately measured.

3. New procedure of calibration of the pattern center

Traditionally, PC location has been calibrated by different methods including feature mirror symmetry methods, screen movement methods or shadow casting methods [18,19]. However, the typical resolution of these methods was of the order of 0.5% of the camera width. With the advent of HR-EBSD this resolution has been shown to be inadequate [15,20] (as it will be demonstrated below) and new PC calibration procedures have been developed. Maurice et al [21], for example, tried to improve the resolution of screen movement methods by cross-correlation techniques but the mechanical insertion/retraction and geometric uncertainties limit its application. Mingard et al. [22] also extended the use of shadow casting techniques with relevant results. Finally, Basinger et al. [23] using an EBSP spherical remapping technique and simulated patterns and reached a resolution of 0.045% in a Ni polycrystal limited by the uncertainty in the exact crystal orientation. In this paper we present a novel method (based on the method proposed by Kacher et al. [13]) with improved resolution that adapts the simulation-based HR-EBSD using GB-DIC procedures to the problem of PC calibration with minimum assumptions on the stress state of the crystal.

3.1. Projective transformation in EBSD

As commented above, an inaccurate calibration of the location of the pattern center (PC) may lead to phantom stresses in HR-EBSD, especially when considering a simulation-based approach. Fortunately, the exact phantom elastic strains derived from errors in the location of the pattern center can be analytically calculated [20]. The projective transformation associated to an EBSD measurement thus implies that any point (X_1^D, X_2^D) in the 2D EBSP is uniquely associated to a 3D crystal direction (defined in the reference frame of the detector) as follows:

$$\left(X_1^D, X_2^D\right) = P_D(u_1,u_2,u_3) = \left(\frac{u_1}{u_3}D, \frac{u_2}{u_3}D\right) \tag{3}$$

or, using Einstein's notation:

$$X_i^D = \frac{u_i}{u_3}D\,; \quad i \in \{1,\,2\} \tag{4}$$

where P_D is the projective transformation, D is the distance between the detector and the sample, and u_i are the coordinates of the crystal direction. If the source (sample) location is moved along

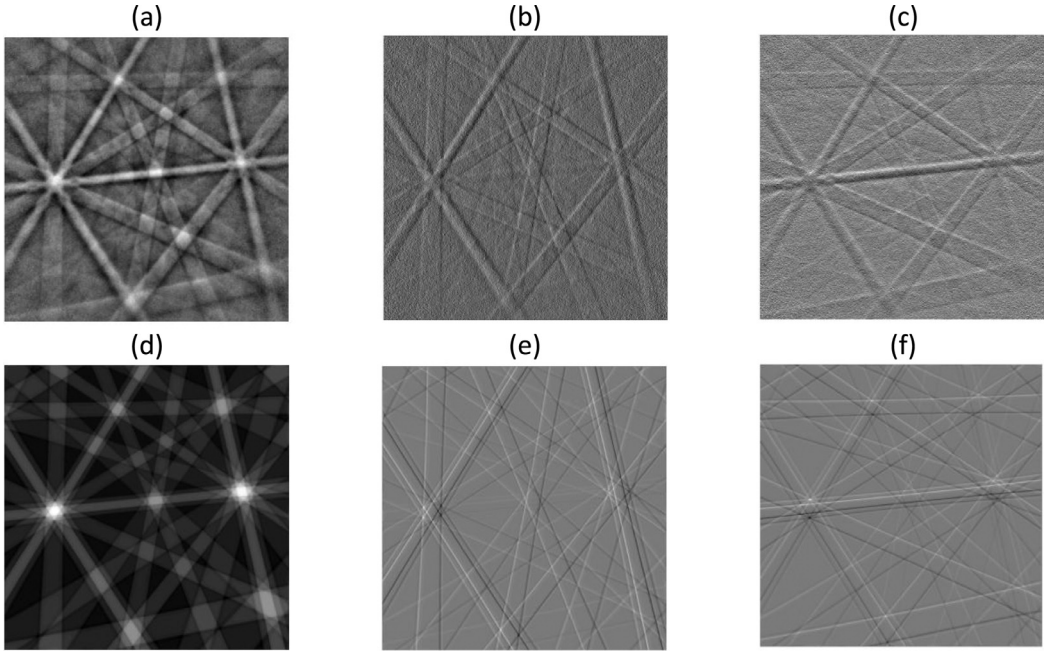

Fig. 1. EBSP image (a) and the corresponding fitted EBSP simulation (d) of the beta phase of the Ti-12wt.%Mo alloy. (b), (e) and (c), (f) correspond to the x and y image gradients of, respectively, real and simulated EBSPs.

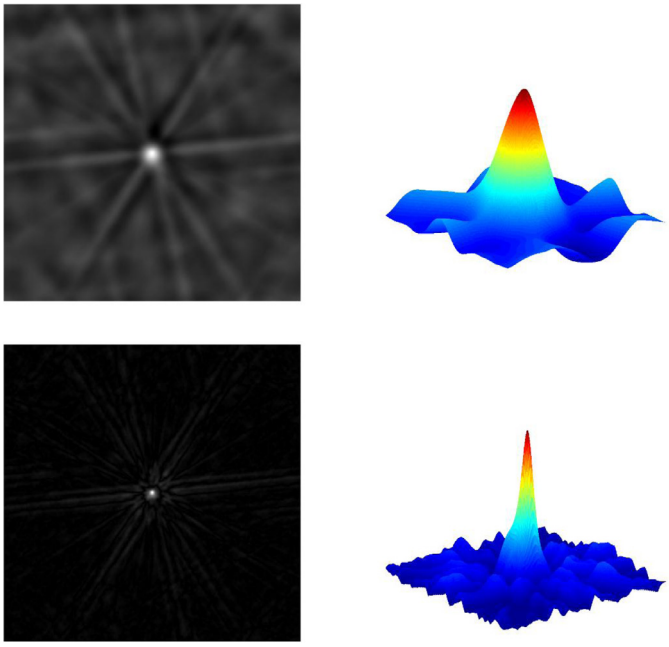

Fig. 2. Above, correlation image (left) between real and simulated patterns in Fig. 1 and a detail of the intensity profile around the maximum (right) using the direct correlation procedure. Below, idem using a gradient-based approach.

a certain direction by $(\Delta_1, \Delta_2, \Delta_3)$, the new corresponding point on the EBSD pattern will be:

$$T_\Delta\left[X_i^D\right] = X_i^D\left(1+\frac{\Delta_3}{D}\right)+\Delta_i \;\; ; \;\; i\in\{1,\,2\} \tag{5}$$

i.e., the EBSD pattern will be expanded/contracted by a factor of $1+\Delta_3/D$ and then shifted by (Δ_1, Δ_2).

On the other hand, if a certain distortion (defined as $\bar{u}_i = F_{ij}u_j$) is applied on the crystal, the new corresponding point in the detector's plane will be:

$$\bar{X}_i^D = \frac{\bar{u}_i}{\bar{u}_3}D = \frac{F_{ij}u_j}{F_{3k}u_k}D \;\; ; \;\; i\in\{1,\,2\} \;\; ; \;\; j,k\in\{1,\,2,\,3\} \tag{6}$$

Combining (4) and (6), we obtain:

$$\frac{\bar{X}_i^D}{D} = \frac{F_{ij}X_j^D + F_{i3}D}{F_{3k}X_k^D + F_{33}D} \;\; ; \;\; i,j,k\in\{1,\,2\} \tag{7}$$

or, in the case of small strain approximation ($F_{ij}=\delta_{ij}+U_{ij}$; with $U_{ij}<<1$):

$$\bar{X}_i^D \cong (1-U_{33})X_i^D + U_{ij}X_j^D + U_{i3}D - U_{3k}X_k^DX_i^D \;\; ; \;\; i,j,k\in\{1,\,2\} \tag{8}$$

It is straightforward to see that in the case of hydrostatic lattice distortions $F_{ij}=(1+U_{hyd})\delta_{ij}$, the EBSD pattern remains invariant ($\bar{X}_i^D = X_i^D$) (at least with respect to the location of the Kikuchi band centers). On the other hand, if we consider only non-trivial F_{i3} components, i.e.:

$$F = \begin{pmatrix} 1 & 0 & F_{13} \\ 0 & 1 & F_{23} \\ 0 & 0 & F_{33} \end{pmatrix} \tag{9}$$

then,

$$\bar{X}_i^D = \frac{1}{F_{33}}\left[X_i^D + F_{i3}D\right] \;\; ; \;\; i\in\{1,\,2\} \tag{10}$$

i.e., the EBSD pattern will be shifted in the plane by $(F_{13}D,\, F_{23}D)$ and then expanded/contracted by a factor of $1/F_{33}$. It is a similar effect as a source (sample) shift.

Therefore, if we combine a F_{i3}-type distortion with a simultaneous sample shift Δ_i, we get:

$$T_\Delta\left[\bar{X}_i^D\right] = \frac{1+\Delta_3/D}{F_{33}}\left[X_i^D + F_{i3}D\right]+\Delta_i \;\; ; \;\; i\in\{1,\,2\} \tag{11}$$

We can construct the following combinations of distortions and sample shifts that maintain the EBSD pattern invariant:

$$\begin{aligned} \Delta_1 &= -F_{13}D \\ \Delta_2 &= -F_{23}D \\ \Delta_3 &= (F_{33}-1)D \end{aligned} \tag{12}$$

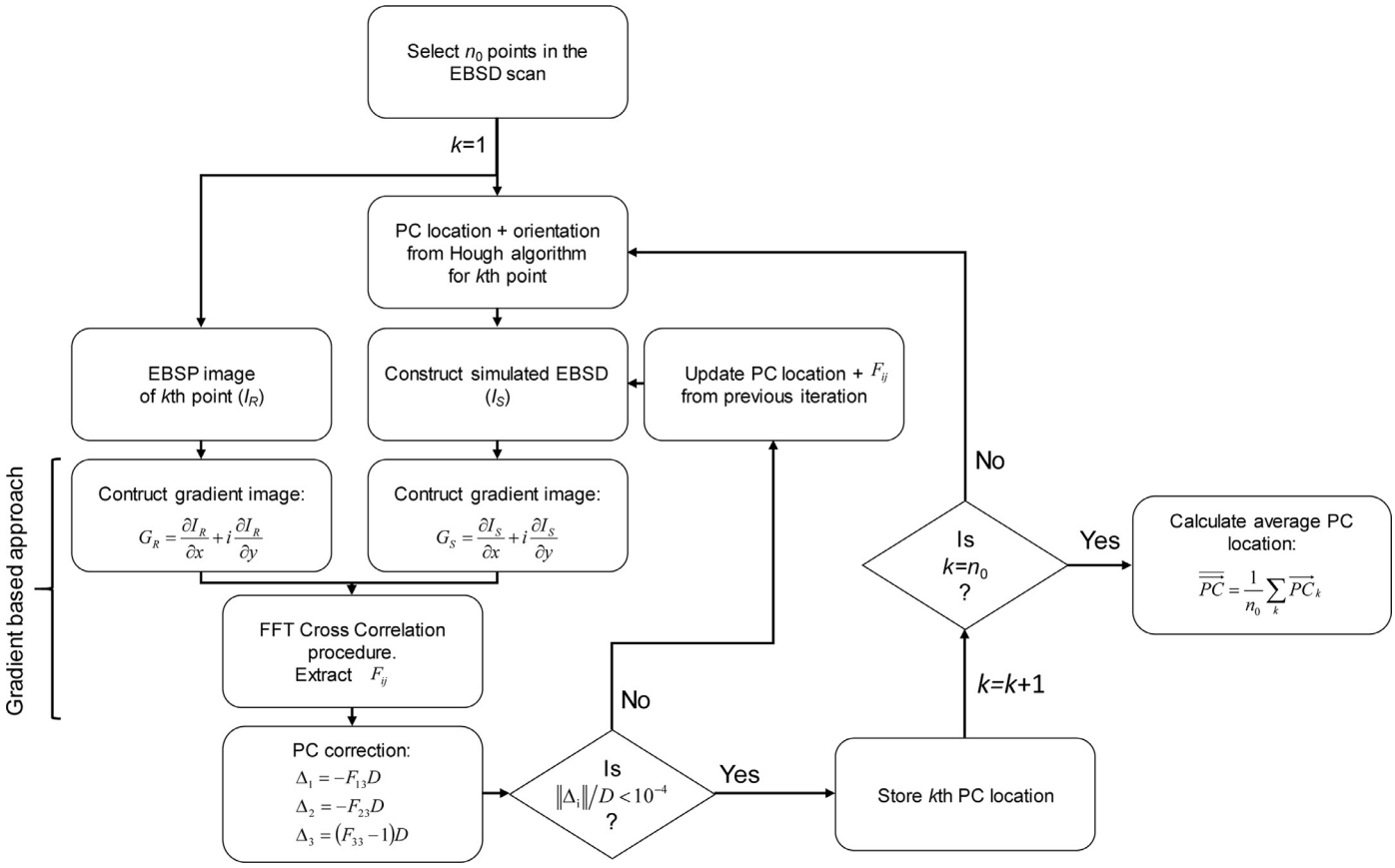

Fig. 3. Schematic description of the PC calibration procedure.

It should be emphasized that this analysis deals with the position of the Kikuchi band centers while any crystal distortion (F_{ij}) has also a true (but negligible) second order effect on the width of the Kikuchi bands. For example, elastic strains will change the interplanar distance by a factor of the order of the applied strain ε that will induce shifts in the Kikuchi lines of the order of $D\theta_{hkl}\varepsilon$, which is about θ_{hkl} times (~one order of magnitude) smaller than their effect on the band center location.

In summary, the problem of extracting the 12 ° of freedom (the 9 F_{ij} components together with the 3 components of the PC location derived fromΔ_i) through the analysis of a single EBSD pattern is ill-conditioned so that 4 further assumptions have to be made.

3.2. New calibration procedure

The aforementioned analysis showed that only 4 assumptions are required in order to solve the whole problem. Three of them can be set assuming that the out-of-plane stress components (σ_{i3}) in the sample reference frame have to be null (free surface assumption). The determination of the last degree of freedom related to the hydrostatic stress in the sample ($\sigma_{11}+\sigma_{22}$ since $\sigma_{33}=0$) will bring to the complete determination of the location of the PC as well as of the whole deformation gradient. Note however that, as EBSD measurement involves an effective interaction volume (it is not strictly a surface measurement), the free surface assumption is not generally valid if strong stress gradients are expected beneath the surface.

It is worth noting that while F_{ij} components (orientations and microstrains) are supposed to strongly vary from point-to-point (especially in polycrystalline materials), the source position is practically static (apart from a slight shift due the electron beam shift and inclination of the sample that can be easily estimated). As a consequence, if reasonable assumptions can be made about the overall mean biaxial stress state ($\sigma_{11}+\sigma_{22}$) (for example by measuring the macroscopic mean surface stress through other alternative techniques such as X-ray diffraction),Δ_i can be fixed in such a way that the mean stresses measured at the different sample crystallites fit the required macroscopic biaxial stress state.

The aforementioned limitations make simulation-based HREBSD only suitable for low to moderately strained crystals, where free surface assumption can be fulfilled and a reasonable assumption can be made for the biaxial stress state.

In the present work two different materials have been considered to validate the proposed techniques. In the case of Si single crystal, the lattice is expected to be relaxed. In the case of the Ti-12wt.% Mo alloy, the sample has been slightly strained in tension up to a plastic strain of about 2%. Thus, a reasonable guess for both cases is that the mean surface biaxial stress is null ($\sigma_{11}+\sigma_{22}=0$) in the interior of the grains.

A novel procedure for PC calibration is thus proposed as described below (see Fig. 3).

(1) Select a set of sample points from which an average PC location will be calculated.
(2) For a given sample point, both the PC location and an approximated crystal orientation are obtained through the conventional Hough algorithm.
(3) A kinematic EBSD pattern is simulated for the PC location and crystal orientations of step 1.
(4) The strain gradient tensor in the detector's coordinate system is calculated with the HR-EBSD procedure.
(5) Considering the relationship between PC location errors and phantom F_{ij} components in the detector's reference system (Eq. (12)), the set of (Δ_1, Δ_2, Δ_3) that fulfills the 4 con-

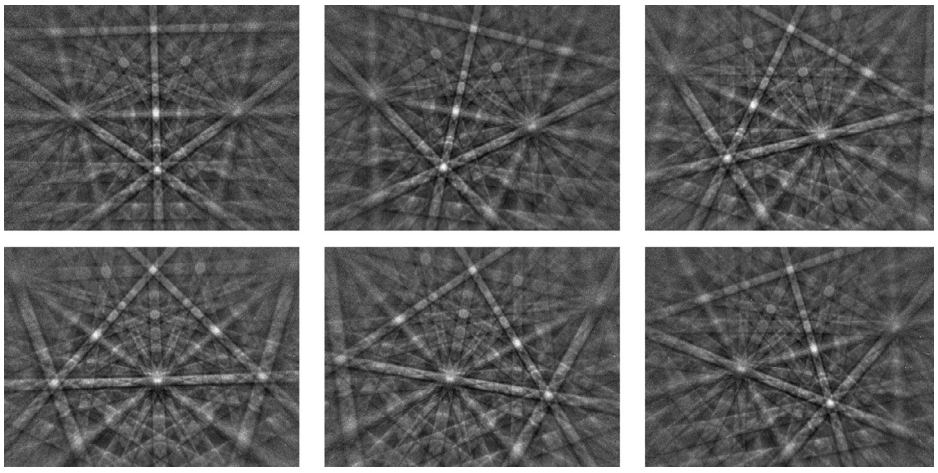

Fig. 4. Kikuchi pattern of each of the considered orientations for the Si single crystal.

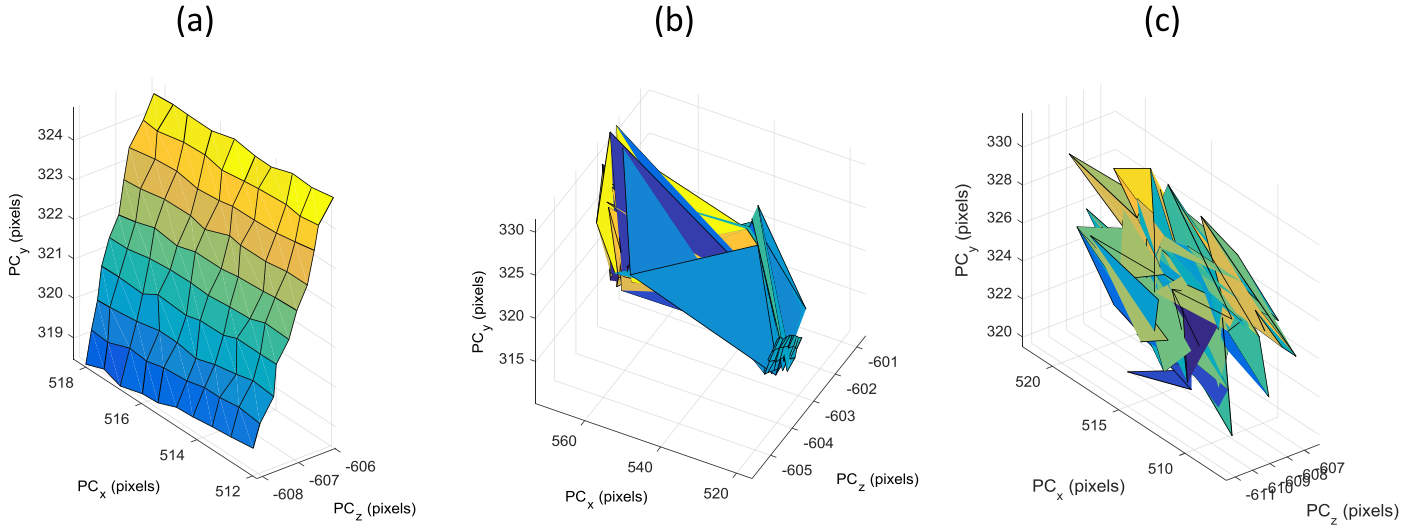

Fig. 5. Based on the procedure of calibration of the PC described in Fig. 3, reconstruction of the sample plane as calculated from the PCx, PCy and PCz (DD) values of the 10×10 scan: (a) using gradient-based approach of kinematic simulations; (b) using simple kinematic simulations; (c) using the standard procedure for PC calibration. (Orientation #2).

straints (free surface approach + null hydrostatic pressure) at the sample's coordinate system are calculated. The corresponding deformation gradient tensor is also calculated.

(6) The new PC location is set from the initial estimation and the calculated(Δ_1, Δ_2, Δ_3).
(7) The new simulated EBSD pattern is constructed for the new PC location and the deformation gradient obtained in step 4.
(8) Steps 4–7 are repeated iteratively until the correction in PC location is below a given threshold.
(9) Proceed with the next sample point (repetition of steps 2–8).
(10) Calculate the average PC location after correcting the possible beam shifts between sample points.

3.3. Validation

The above procedure of calibration of the PC (excluding step 10) was validated for a (100) Si single crystal mounted in a FEG-SEM JEOL JMS 7100F equipped with a NORDLYS II camera. 10×10 EBSPs were acquired covering $135 \times 135\ \mu m^2$ with a step size of $15\ \mu m$ for 6 different crystal orientations. The sample was rotated 15° around the (100) axis between EBSD maps. The aim is to apply the GB-DIC technique following the PC calibration procedure described above in order to verify its robustness for different EBSD patterns. The results were compared with the conventional simulation-based approach (using Bragg simulations) and with the standard PC calibration procedure. As the standard PC calibration in the commercial software is done manually, we have calculated the 10×10 PC values only for crystal orientation #2. Fig. 4 shows a Kikuchi pattern of each of the considered orientations.

Fig. 5 shows the calculated values of PCx, PCy and PCz (or DD) over one of the 10×10 scan. The results show that the proposed procedure (using the gradient-based approach) is able to capture the PC shifts during the electron beam scan. All the PC values were fitted to a rectangular planar grid (the fitted spacing responds to the following correspondance: 0.0456 pixels per micron). The calculated normal axes for each crystal orientation are shown in Table 1; as expected, it varies only slightly from scan to scan since the sample rotation axis is virtually parallel to the grid plane normal. In all the cases the inclination angle of the fitted plane is very close to the nominal sample inclination (70°). Moreover, the deviation of the PC values from the fitted rectangular grid (Fig. 6) are in all cases (for all the 6 different crystal orientations and the 3 PC components) very small with an outstanding standard deviation of the order of 0.1 pixels (less than 0.01% of the screen width).

Table 1
Components of the normal to the fitted plane using the gradient-based approach. Corresponding inclination angle.

Crystal	n_1	n_2	n_3	Inclination (°)
Orientation #1	0.015	−0.346	0.938	69.8
Orientation #2	−0.001	−0.331	0.944	70.7
Orientation #3	0.006	−0.295	0.956	72.8
Orientation #4	0.012	−0.306	0.952	72.2
Orientation #5	−0.015	−0.308	0.951	72.1
Orientation #6	0.027	−0.311	0.950	71.9

It is worth noting that simulation-based HREBSD has an inherent source of error due to the uncertainty in the sample surface orientation. This uncertainty involves an error in the sample tilt and the sample to detector orientation relationship. However, the effect on the calculated stress state or PC calibration is usually negligible. Given an scenario where the uncertainty in the sample tilt is of the order of $\theta = 0.05$ rad ($\sim 3°$) and the crystal is strongly elastically strained $\varepsilon_{ij} = 5 \cdot 10^{-3}$, the effect of this uncertainty in the stress state would be of the order of $\Delta\varepsilon_{ij} \sim \varepsilon_{ij} \sin\theta \approx 2 \cdot 10^{-4}$, around the resolution of the simulation-based HREBSD procedure.

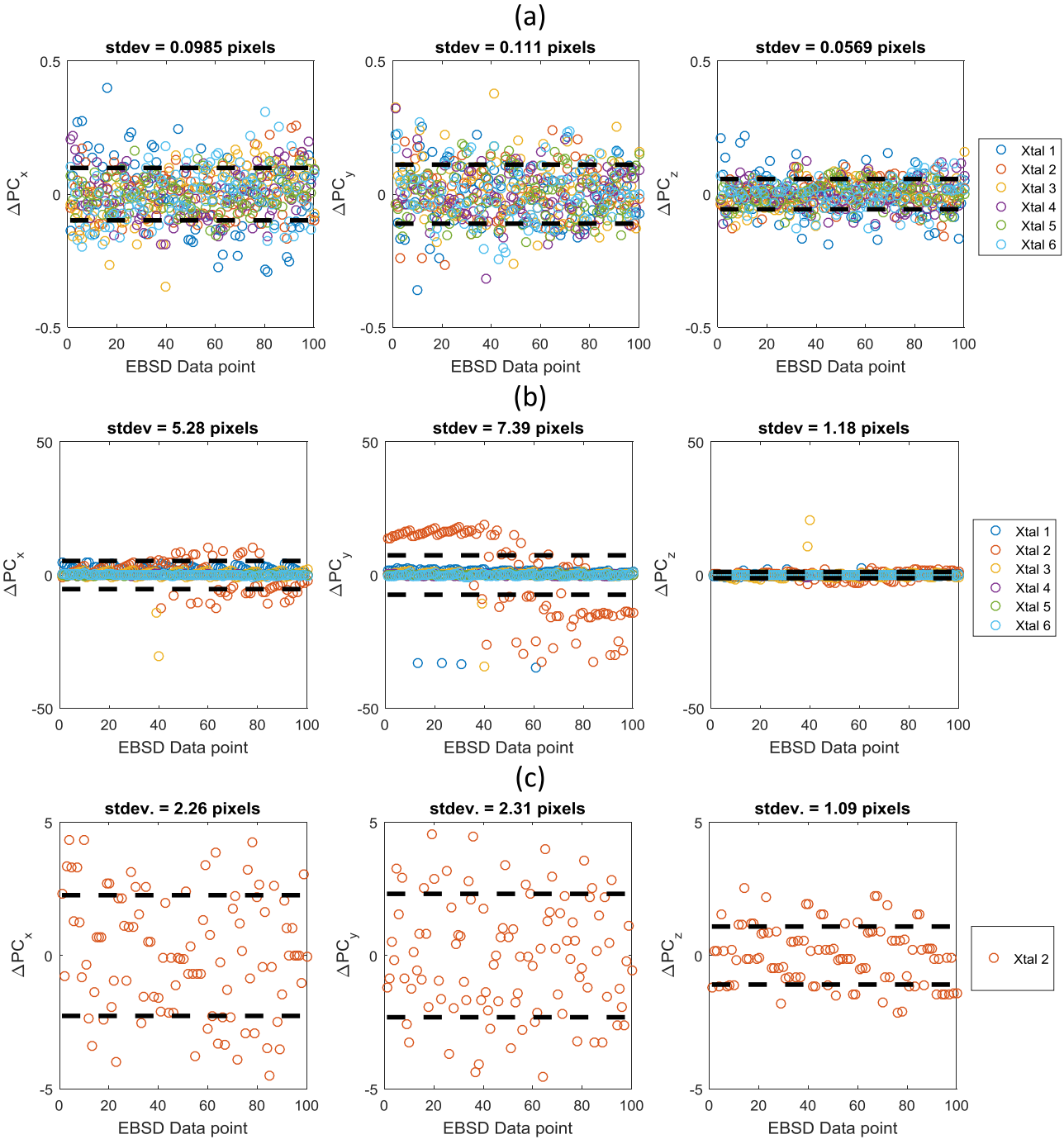

Fig. 6. Based on the PCx, PCy and PCz values obtained from the PC calibration, deviation from fitted grid (in pixels) of each of 10×10 sample points for each of the analyzed crystal orientations. (a) using gradient-based approach (b) using direct approach (no gradient), (c) using the standard procedure for PC calibration (only for crystal orientation #2). Note that different scales are used.

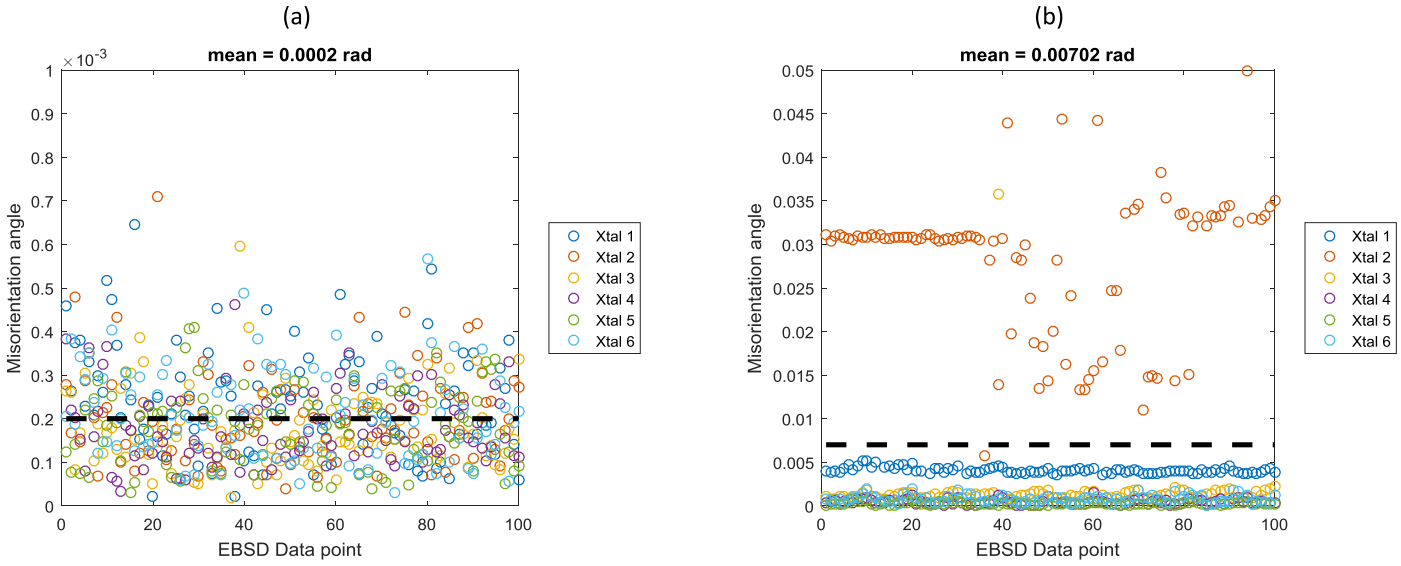

Fig. 7. Misorientation angle (in radians) with respect to the mean crystal orientation for each of the analyzed crystals as calculated using the gradient-based approach (a) and the direct approach (b) dotted line corresponds to the average misorientation value. Note that different scales are used.

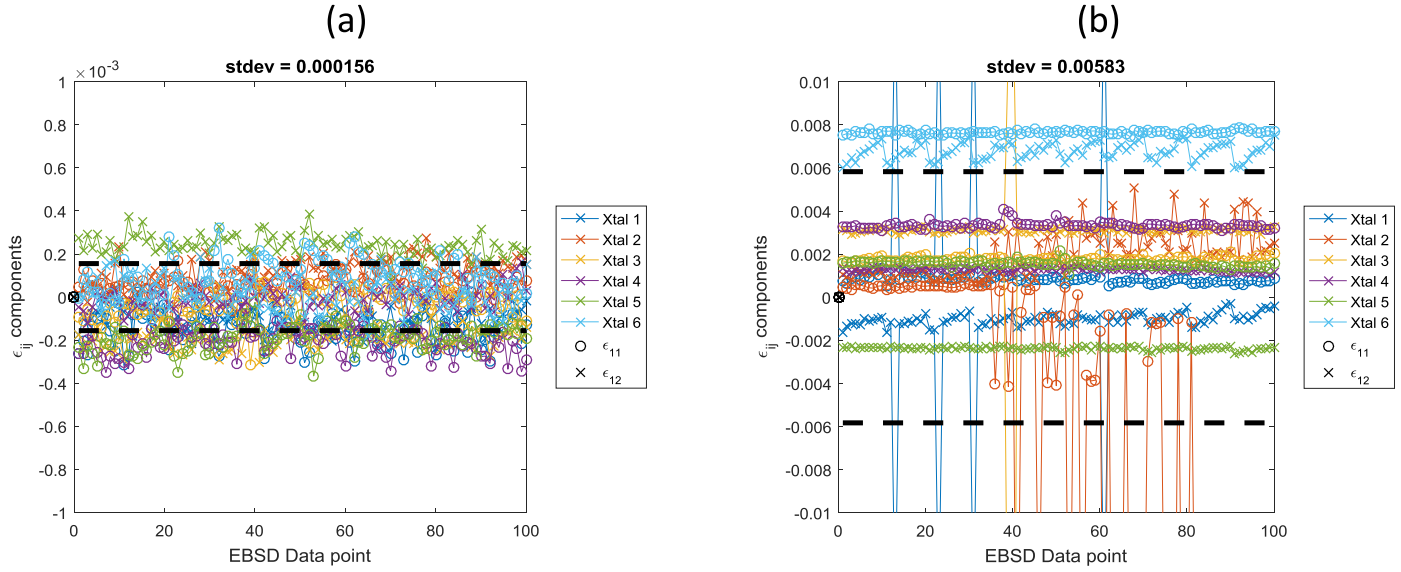

Fig. 8. Independent elastic strain components for each of 10×10 sample points for each of the 6 crystal orientations as calculated using gradient-based approach (a) and direct approach (b) note that different scales are used.

On the other hand, the calculated F_{ij} deformation gradient was decomposed in order to extract the crystal orientation and the elastic strain tensor. Fig. 7 shows the misorientation angle of each of the EBSD scan points with respect to the mean crystal orientation. Again, the average misorientation within every EBSD map is very small ($\sim 2 \times 10^{-4}$ rad) in spite of using kinematical Bragg algorithm to construct the simulated EBSPs.

In addition, Fig. 8 shows the elastic strain components for every EBSD scan point. Although some of the coefficients have been constrained due to the assumptions made, the "free" coefficients are still very low (of the order of $\sim 1-2 \times 10^{-4}$), well corresponding to a stress-free single crystal and confirming the absence of any phantom stresses due to errors in the PC location.

These results are very accurate especially when compared to the conventional DIC techniques, which present three main important limitations unsuitable for accurate HR-EBSD. Firstly, it often leads to unstable results (converging to different solutions for a given crystal orientation, see Fig. 7(b)). Secondly, the repeatability of the results is much poorer than in the gradient-based approach, even in the case of a given stable solution. For instance, the standard deviation of PC location values from the fitted plane is much higher than that for the gradient-based approach (see Fig. 6(b)). Finally, the poor direct fitting ability of simple Bragg simulations induces inaccurate solutions as a result of the aforementioned limitations. This is clearly observed in Fig. 8(b), where the calculated ε_{ij} elastic strain components are presented. The converged solution, although rather repetitive for a given crystal orientation, is incompatible with the stress-free Si single crystal. This means that the solution reached by the conventional simulation-based algorithm is inaccurate.

4. HR-EBSD hybrid model

4.1. Fundamentals

Even if the improvement of the simulation-based algorithm is impressive, it is still not comparable with the accuracy of HR-EBSD algorithms using real EBSD patterns. However, as commented in the introduction, real pattern HR-EBSD algorithms can only measure the relative deformation gradient tensor with respect to a reference sample point.

A new HR procedure is thus needed to measure the F_{ij} deformation gradient tensor of polycrystalline samples in an absolute manner. The new hybrid procedure combines the best characteristics of both strategies in a three step procedure:

(1) The above PC calibration procedure is performed at the interior points of different crystals (where elastic strains are usually lower). Note that due to the assumptions required for this procedure, slightly different PC values might be expected from different crystals specially in highly strained crystals. Thus, in order to minimize the error in the PC calibration, the average value of all the PC locations obtained at many different grains is considered. In this process, PC shifts due to the different scan positions are taken into account and substracted from the PC calibration procedure.
(2) Once PC location is calibrated, a set of points (5–10 points) are selected in the interior of every grain. Again, interior points are preferred since they usually present better EBSP quality and lower elastic strain levels. At each point of the set, simulation-based HR-EBSD is performed (using the gradient-based approach) in order to obtain the absolute stress state and misorientation of each point. Again, as the problem is still ill-conditioned due to the hydrostatic stress component further assumptions have to be made ($\sigma_{33}=0$). Parallelly, the conventional HR-EBSD procedure is performed for each pair of points of the set in order to get in a very accurate manner the relative stress differences and misorientations within each set of points. The information derived from simulation-based approach and the conventional approach is crossed to get an accurate value of the absolute stress state and orientation.
(3) Finally, the conventional HR-EBSD procedure is used to calculate the relative misorientation and stress state for the rest of points in the grain.

The procedure is explained in detail in Fig. 9 and involves the following steps:

(1) In each grain in the EBSD map (analysed using conventional Hough transform algorithms), a set of n0 grain points are selected. The first one will be considered as the reference point within the grain.
(2) For each of the selected grain points (point k), the deformation gradient tensor is computed in two different ways:
   (a) $\Delta F_{ij}^{k,real}$: Relative to the reference (1st) point, following a conventional HR procedure of real EBSD patterns (similar to Wilkinson's approach [3]). In this work, an iterative algorithm is considered, using the image transformation tools of MATLAB®.
   (b) $F_{ij}^{k,simu}$: In an absolute approach, following a gradient-based procedure considering kinematically simulated EBSPs (similar to the one considered in the PC calibration procedure but fixing the PC location calculated previously and assuming that $\sigma_{33}=0$ to correct the hydrostatic pressure).
(3) Once $\Delta F_{ij}^{k,real}$ and $F_{ij}^{k,simu}$ are calculated for each of the n0 selected grain points, their average values are computed: $\overline{\Delta F_{ij}}$ and $\bar{F}_{ij}$, respectively.
(4) It can be easily seen that the absolute deformation gradient tensor of the reference grain point (1st selected point) can be easily recomputed as follows: $F_{ij}^{1}=[(\overline{\Delta F})^{-1}\cdot\bar{F}]_{ij}$. The use of an average $\bar{F}_{ij}$ (instead of a single measurement) extracted from simulation based HR-EBSD warrants a better accuracy of the obtained solution. The average $\bar{F}_{ij}$ is calculated as follows: first, each F_{ij}^{k} is decomposed by a *RU* polar decomposition ; then, the average orientation $\bar{R}$ is calculated in the quaternion representation and extracted from the total deformation gradient to get the strain-related tensor: $\hat{U}^{k}=\bar{R}^{T}R^{k}U^{k}$; finally, as the absolute values of $\hat{U}_{ij}^{k}$ components are expected to be very small (they are purely related to the elastic strain state of each point), a simple arithmetic average is performed so that: $\bar{F}=\bar{R}\bar{U}=\bar{R}(\frac{1}{n_0}\sum_{k}\hat{U}^{k})$. The same procedure is followed for $\overline{\Delta F_{ij}}$.
(5) The conventional HR procedure (comparing real EBSPs with the reference EBSP of point 1) is applied to every point in the selected grain to extract ΔF_{ij}^{k}.
(6) The absolute deformation gradient of each point is computed from the result of steps 4 and 5: $F_{ij}^{k}=\Delta F_{ij}^{k}\cdot F_{ij}^{1}=\Delta F_{ij}^{k}\cdot(\overline{\Delta F_{ij}})^{-1}\cdot\bar{F}_{ij}$
(7) Once all the points in the grain have been analyzed, steps 1–6 are repeated for each grain in the EBSD map.

The proposed procedure assumes that the sample surface is totally flat. If differential polishing induces excessive height changes this will affect the strain measurements as can be deduced from Eq. (8). As a rule of thumb, a change in height of the order of 10^{-4} times DD (typically some microns) will induce phantom strains of the order of 10^{-4}.

4.2. Application to strain-induced martensite lath in a metastable β-Ti alloy

The novel approach described above has been used to analyze the martensitic transformation induced by plastic deformation in an as-quenched Ti-12wt.%Mo alloy [24].

Metastable β-Ti alloys attract more and more attention due to their unique combination of properties such as excellent strength-to-weight ratio and corrosion resistance [25]. Their wide range of achievable properties are well adapted to specific use as aeronautic and/or biomedical materials. Moreover, recent alloy-by-design strategy brought new insight in the improvement of the strain-hardening rate, which is frequently the weak point of β-Ti alloys [24,26,27]. Owing to this strategy, new Ti grades were proposed exhibiting simultaneously mechanical $\{332\}<113>$ twinning and α'' strain-induced martensitic (SIM) transformation [24,28]. This combination of plastic deformation mechanisms leads to previously unreached strain-hardening rates for titanium alloys. However, the contribution of each mechanism is still unclear, and is still under investigations.

To illustrate the effectiveness of this new HR-EBSD approach, a slightly plastically strained sample of a metastable β Ti-12wt.%Mo sample has been investigated. The experimental procedure is depicted in [28]. The sample has been deformed up to $\varepsilon=0.02$ and then mounted in conductive resin for EBSD preparation. Mechanical polishing with SiC papers followed by diamond polishing down to 3 µm particles size has been performed. Final polishing with H_2O_2-added colloidal suspension of oxide particles of 0.05 µm was applied to reach the surface state needed for correct EBSD measurements.

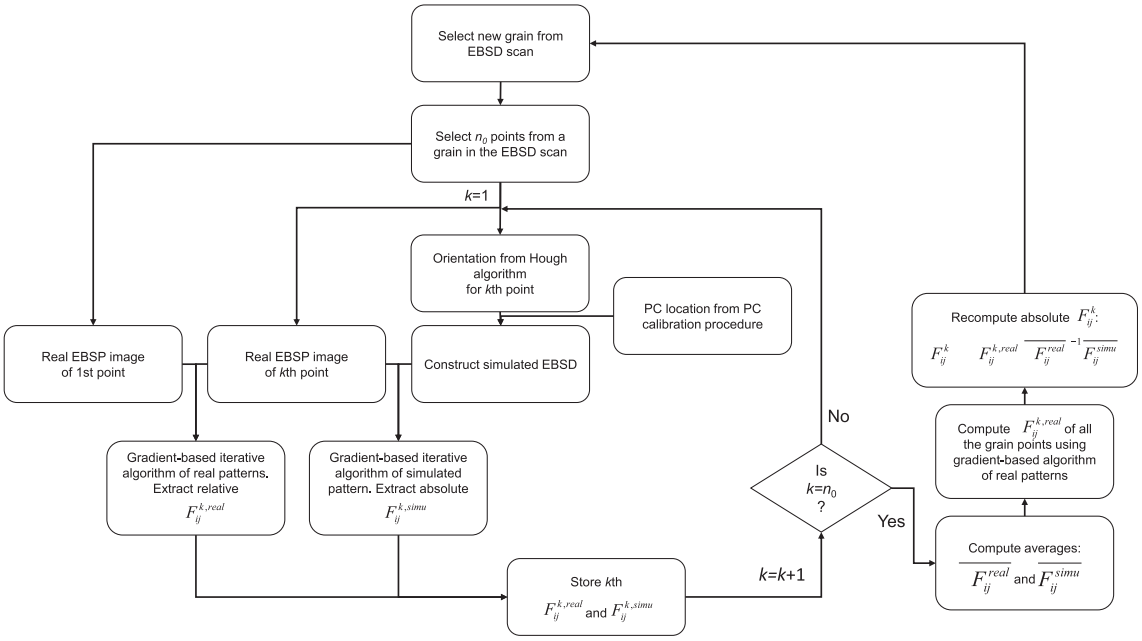

Fig. 9. Schematic description of the hybrid HR-EBSD procedure.

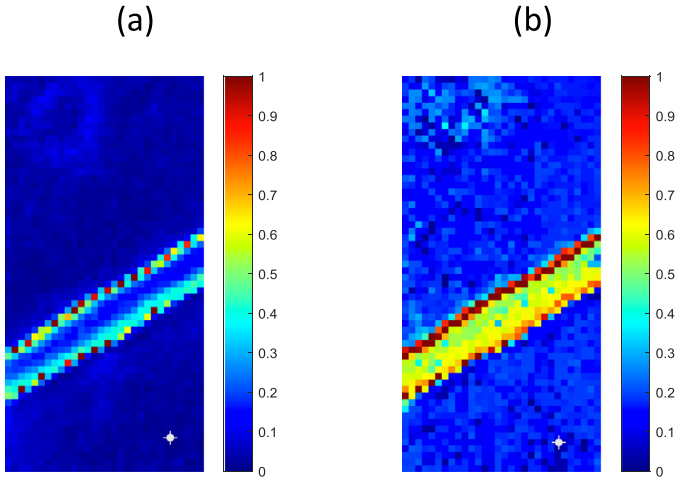

Fig. 10. Misorientation angle maps with respect to the orientation of the reference point highlighted in grey. (a) using the proposed HR procedure. (b) using the conventional procedure by HKL Channel 5 software. Step size: 150 nm.

According to the literature [29], the orientation relationship (OR) between the β-Ti and the martensitic phase (α") corresponds to:

$$\begin{matrix} [001]_{\alpha''} // \left[\bar{1}\bar{1}0\right]_{\beta} \\ \left[\bar{1}\bar{1}0\right]_{\alpha''} // \left[1\bar{1}\bar{1}\right]_{\beta} \\ \left(1\bar{1}0\right)_{\alpha''} // \left(1\bar{1}2\right)_{\beta} \end{matrix} \tag{13}$$

However, the accommodation of the different lattice structures in the neighborhood of the β-α" strain-induced interfaces is, to the best of our knowledge, still unknown. The novel hybrid HR-EBSD approach introduced in this work, enabling the determination in an absolute manner both the crystal orientation and the elastic strain state, was applied both to identify the exact OR and to highlight the accommodation around the interphases. The results were also compared with the commercial EBSD analysis procedure (HKL Channel 5 Flamenco v5.0.9.0).

Fig. 10 shows the misorientation angle with respect to a sample point (highlighted in white) in the interior of the β-Ti phase containing a SIM α" lath. The misorientation angle in the interior of the α" martensite has been calculated assuming the ideal OR described in Eq. (13). The results show finer misorientation resolution in the HR procedure as expected. Moreover, the HR results show that the ideal OR is maintained in the interior of the two phases whereas there is a misorientation of about 0.3–0.5° in the neighborhood of the two boundaries.

One might deduce that as the misorientation is similar on both sides of the boundaries, the OR is also maintained at these boundaries. However, thanks to the improved angular resolution it is possible resolve the misorientation axis with good accuracy. Thus, if we consider the corresponding unit quaternion defined as:

$$\bar{q} = \begin{pmatrix} q_x \\ q_y \\ q_z \\ q_w \end{pmatrix} = \begin{pmatrix} \omega_x \sin(\theta/2) \\ \omega_y \sin(\theta/2) \\ \omega_z \sin(\theta/2) \\ \cos(\theta/2) \end{pmatrix} \tag{14}$$

where $(\omega_x, \omega_y, \omega_z)$ is the related rotation axis and θ is the misorientation angle, we observe that the rotation axis at the two sides of the interphase boundary present opposite signs, especially for the upper grain boundary (left boundary in Fig. 11). This means that OR is not maintained in the neighborhood of the interphase boundary. Again, the results show that only with the improved resolution of the HR approach is possible to determine the misorientation axis.

With regard to the elastic distortion, Fig. 12 shows the elastic strain components (at the sample's reference frame as a function to the distance to the center of the α" martensitic lath. The results again show that stress components have opposite signs at both sides of a given interphase boundary. The high levels of elastic strains in α" martensitic lath may be due to two possible contributions: (1) Real elastic strains in the lattice; (2) A mismatch in the input lattice parameters (orthorrhombic). Unfortunately, it is difficult to discriminate which of them is dominant.

In absolu, the two crystals seem to be oriented and stressed in opposite directions around the boundaries; this probably indicates a strong dislocation activity of opposite sign at the two sides of the interphase boundary.

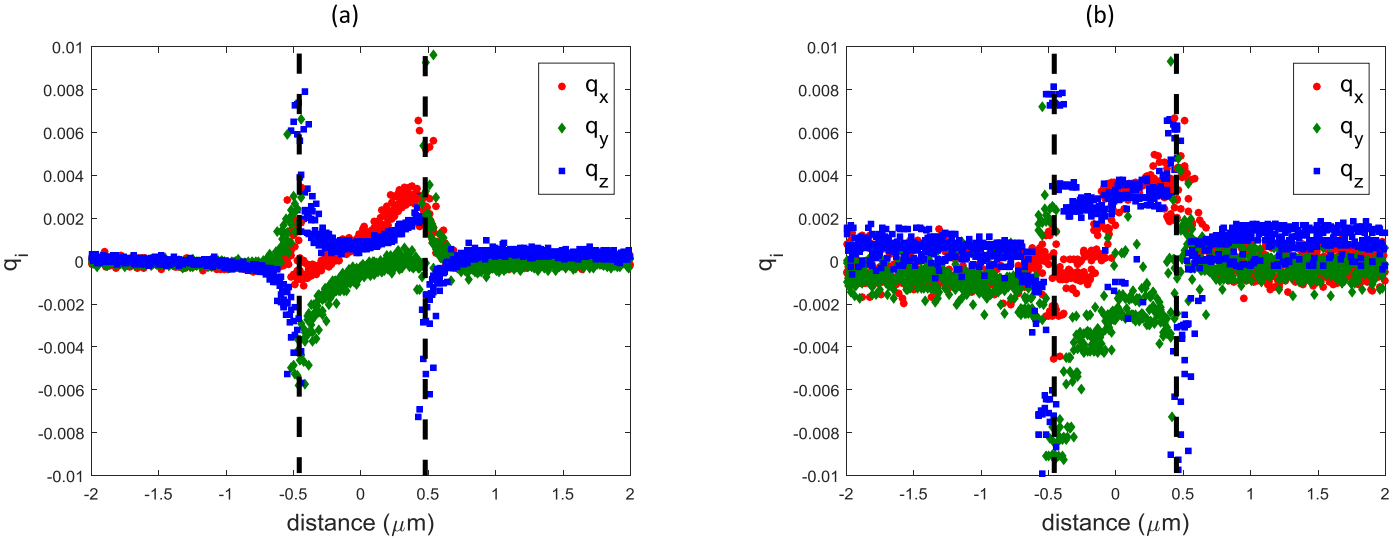

Fig. 11. Evolution of the qx, qy and qz components of the unit quaternion (see Eq. (14)) corresponding to the misorientation with respect to the reference sample point indicated in Fig. 10, vs the distance to the center of the a" martensitic lamella. (a) using the proposed HR procedure. (b) using the conventional procedure by HKL Channel 5 software. Black dash line indicates the position of grain boundaries.

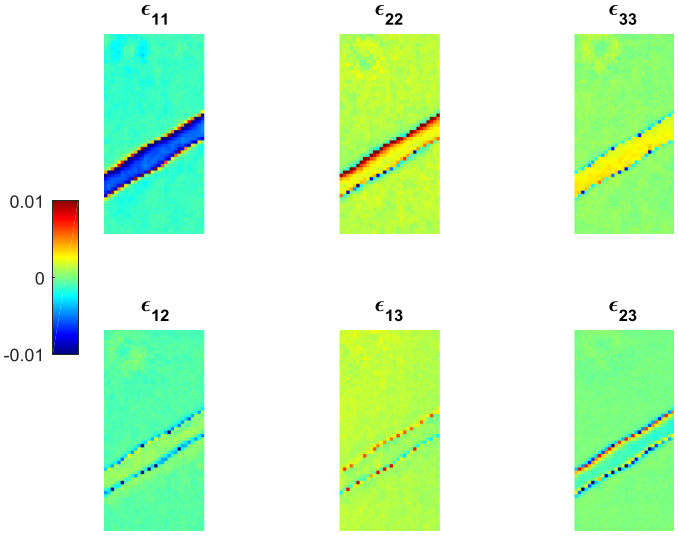

Fig. 12. Elastic strain map at the reference frame of the sample. Step size = 150 nm.

Note that these results are only accessible with the hybrid HR procedure (where absolute orientations can be determined) since two different crystal phases are being compared. A deeper analysis of these results is in progress.

5. Conclusions

A novel gradient based DIC technique (GB-DIC) for the cross-correlation between real and simulated EBSPs has been proposed that improves the accuracy and robustness of simulation based HR-EBSD procedure. As a consequence, a new procedure of calibration of the pattern center was designed using the GB-DIC, assuming minimum assumptions. This procedure of PC calibration was applied using GB-DIC and the conventional DIC. GB-DIC based algorithm showed improved consistency and accuracy in a set of 6 different Si single crystal orientations and led to remarkable results in the accurate determination of the pattern center location.

The emergence of this accurate simulation-based HR-EBSD brings the absolute determination with high resolution of both orientations and elastic strains from EBSPs. This is of great interest in the analysis of special boundaries as twin boundaries or interphase boundaries. In this work, a hybrid approach is proposed that combines the simulation based HR-EBSD with the conventional HR-EBSD (Wilkinson's procedure) and was successfully applied to the analysis of a β/α" interface in a Ti-12wt.%Mo alloy.

Acknowledgment

The authors gratefully acknowledge the support of the inter-university attraction poles (IAP) Programme P7/21, project INTEMATE, funded by the Belgian State, Belgian Science Policy.

References

[1] N.C. Krieger-Lassen, K. Conradsen, D. Juul-Jensen, Image-processing procedures for analysis of electron back scattering patterns, Scanning Microsc. 6 (1992) 115–121.
[2] A.J. Schwartz, M. Kumar, B.L. Adams, Electron backscatter diffraction in materials science, Kluwer Academic/Plenum Publishers, New York, 2000.
[3] A.J. Wilkinson, G. Meaden, D.J. Dingley, High resolution mapping of strains and rotations using electron backscatter diffraction, Mater. Sci. Technol. 22 (2006) 1271–1278.
[4] A.J. Wilkinson, G. Meaden, D.J. Dingley, High-resolution elastic strain measurement from electron backscatter diffraction patterns: new levels of sensitivity, Ultramicroscopy 106 (2006) 307–313.
[5] A.J. Wilkinson, E.E. Clarke, T.B. Britton, P. Littlewood, P.S. Karamched, High-resolution electron backscatter diffraction: an emerging tool for studying local deformation, J. Strain Anal. Eng. Des. 45 (2010) 365–376.
[6] T.B. Britton, A.J. Wilkinson, Measurement of residual elastic strain and lattice rotations with high resolution electron backscatter diffraction, Ultramicroscopy 111 (2011) 1395–1404.
[7] C. Maurice, R. Fortunier, A 3D hough transform for indexing EBSD and Kossel patterns, J. Microsc. 230 (2008) 520–529.
[8] N. Isasti, D. Jorge-Badiola, J. Alkorta, P. Uranga, Analysis of complex steel microstructures by high-resolution EBSD, JOM 68 (2016) 215–223.
[9] T.B. Britton, A.J. Wilkinson, High resolution electron backscatter diffraction measurements of elastic strain variations in the presence of larger lattice rotations, Ultramicroscopy 114 (2012) 82–95.
[10] C. Maurice, J.H. Driver, R. Fortunier, On solving the orientation gradient dependency of high angular resolution EBSD, Ultramicroscopy 113 (2012) 171–181.
[11] S. Villert, C. Maurice, C. Wyon, R. Fortunier, Accuracy assessment of elastic strain measurement by EBSD, J. Microsc. 233 (2009) 290–301.
[12] J. Kacher, C. Landon, B.L. Adams, D. Fullwood, Bragg's law diffraction simulations for electron backscatter diffraction analysis, Ultramicroscopy 109 (2009) 1148–1156.
[13] J. Kacher, Cross-Correlation-Based Texture Analysis Using Kinematically Simulated EBSD Patterns PhD Thesis, Brigham Young University, 2009.
[14] D. Fullwood, Mark Vaudin, C. Daniels, T. Ruggles, S.I. Wright, Mater. Characterization 107 (2015) 270–277.

[15] T.B. Britton, C. Maurice, R. Fortunier, J.H. Driver, A.P. Day, G. Meaden, D.J. Dingley, K. Mingard, A.J. Wilkinson, Factors affecting the accuracy of high resolution electron backscatter diffraction when using simulated patterns, Ultramicroscopy 110 (2011) 1443–1453.
[16] A. Winkelmann, C. Trager-Cowan, F. Sweeney, A.P. Day, P. Parbrook, Many-beam dynamical simulation of electron backscatter diffraction patterns, Ultramicroscopy 107 (2007) 414–421.
[17] G. Tzimiropoulos, V. Argyriou, S. Zafeiriou, T. Stathaki, Robust FFT-based scale-invariant image registration with image gradients, IEEE Trans. Pattern Anal. Mach. Intell. 32 (2010) 1899–1906.
[18] A.P. Day, Developments in the EBSP Technique and its Application to Grain Imaging, PhD Thesis, University of Bristol, 1993.
[19] S. Biggin, D.J. Dingley, A general method for locating the X-ray source point in Kossel diffraction, J. Appl. Cryst. 10 (1977) 376–385.
[20] J. Alkorta, Limits of simulation-based high resolution EBSD, Ultramicroscopy 131 (2013) 33–38.
[21] C. Maurice, K. Dzieciol, R. Fortunier, A method for accurate localisation of EBSD pattern centres, Ultramicroscopy 111 (2011) 140–148.
[22] K. Mingard, A. Day, C. Maurice, P. Quested, Towards high accuracy calibration of electron backscatter diffraction systems, Ultramicroscopy 111 (2011) 320–329.
[23] J. Basinger, D. Fullwood, J. Kacher, B. Adams, Pattern center determination in electron backscatter diffraction microscopy, Microsc. Microanal. 17 (2011) 330–340.
[24] M. Marteleur, F. Sun, T. Gloriant, P. Vermaut, P.J. Jacques, F. Prima, On the design of new β-metastable titanium alloys with improved work hardening rate thanks to simultaneous TRIP and TWIP effects, Scr. Materialia 66 (2012) 749–752.
[25] C. Leyens, M. Peters, Titanium and Titanium Alloys, Wiley-VCH, Weinheim, 2003.
[26] F. Sun, J.Y. Zhang, M. Marteleur, C. Brozek, E.F. Rauch, M. Veron, P. Vermaut, P.J. Jacques, F. Prima, A new titanium alloy with a combination of high strength, high strain hardening and improved ductility, Scr. Materialia 94 (2015) 17–20.
[27] C. Brozek, F. Sun, P. Vermaut, Y. Millet, A. Lenain, D. Embury, P.J. Jacques, F. Prima, A β-titanium alloy with extra high strain-hardening rate: design and mechanical properties, Scr Materialia 114 (2016) 60–64.
[28] F. Sun, J.Y. Zhang, M. Marteleur, T. Gloriant, P. Vermaut, D. Laillé, P. Castany, C. Curfs, P.J. Jacques, F. Prima, Investigation of early stage deformation mechanisms in a metastable β titanium alloy showing combined twinning-induced plasticity and transformation-induced plasticity effects, Acta Materialia 61 (2013) 6406–6417.
[29] J.P. Morniroli, M. Gantois, Etude des conditions de formation de la phase omega dans les alliages titane-niobium et titane-molybdène, Mem, Sci. *Rev. Metal* 11 (1973) 831–842.